Sulfur-Doped Carbon-Wrapped Heterogeneous $Fe_3O_4/Fe_7S_8/C$ Nanoplates as Stable Anode for Lithium-Ion Batteries

Kang Chen,[a] Xiangzhong Kong,[a, c] Xuefang Xie,[a] Jing Chen,[a] Xinxin Cao,[a] Shuquan Liang,[a] and Anqiang Pan*[a, b]

High-capacity electrode materials have attracted tremendous attention in energy storage systems. However, the large volume expansion always causes breakdown of electrode materials and capacity fading. In this work, we report the preparation of heterogeneous $Fe_3O_4/Fe_7S_8/C$ nanoplates with a high lithium diffusion coefficient and excellent lithium storage performance. The heterogeneous nanoplates can be derived from Fe-MOF octahedra during the sulfidation process. As an anode for lithium-ion batteries, the $Fe_3O_4/Fe_7S_8/C$ composite exhibits higher specific capacity and better rate capability than Fe_3O_4/C and Fe_7S_8/C counterparts. The $Fe_3O_4/Fe_7S_8/C$ nanoplates deliver a reversible capacity of 859 mA h g^{-1} after 100 cycles at 0.1 A g^{-1}. Even at 2 A g^{-1}, a capacity of 549 mA h g^{-1} can still be remained. The good performances are attributed to the small nanocrystallites, high surface area, and the heterogeneous phase boundaries. The strategy can be potentially applied to other metal oxide/metal sulfide composite phases or even bimetallic sulfides and bimetal oxides for high performance lithium-ion batteries.

1. Introduction

Developing sustainable and efficient environmental friendly energy storage systems and devices are becoming urgent due to the increasing environmental pollutions and energy demand.[1–3] Lithium-ion batteries (LIBs) are considered to be promising energy storage devices and have been widely used in portable communication equipment, electric vehicles and military fields because of their high capacity, long lifespan and environmental friendly.[4] However, the energy density of lithium ion battery has meet the bottle-neck and is largely dependent on the innovation of electrode materials. The state-of-art graphite anode material owns relatively low theoretical capacity (372 mA h g^{-1}), which cannot meet the needs of higher energy/power densities. Therefore, the development of alternative anode materials with high capacity is the key to the next-generation LIBs.

In recent years, transition metal oxides and transition metal sulfides are considered as potential anode materials for LIBs due to their high theoretical capacity. In particular, iron-based compounds have attracted extensive attention due to their high theoretical capacity, low cost and environmental benignity.[5–6] Iron oxides and iron sulfides are widely studied as anode materials of LIBs.[7] However, its electrochemical performances are limited by their large volume expansion during Li$^+$ up-take and removal process, which results in the capacity fading and structural degraded.

Many efforts have been devoted to build unique nanostructures or making composites to alleviate volume expansion and improve the structural stability, thus resulting enhanced electrochemical performances. To date, various structures, such as nanobiscuits,[8] flowerlike,[9] nanorods,[10] shuttle-like[11] and 3D interconnected FeS@Fe₃C@graphitic carbon networks[12] have been reported. In these works, the nanostructures can better release the stress, increase the contact area between active-material/electrolyte and shorten the ion diffusion path, leading to improved electrochemical performance of iron sulfide as the anode materials for LIBs.[13–18] More recently, the construction of heterogeneous composites has been proven to be an effective strategy to obtain good electrochemical properties.[19–20] Numerous external defects and active sites for rapid electron and ion transport can be produced at these phase boundaries, which is helpful to the lithium ions diffusion.[21–22] Partial sulfurization of iron oxide to produce the heterogeneous iron oxide/iron sulfide composite may improve its electrochemical performance because iron sulfide exhibits smaller band-gap energy than pure iron oxide, thereby improving the electronic conductivity of iron oxide. Moreover, iron oxide and iron sulfide have different lithium insertion/desertion potentials, thus the overall volume expansion during

[a] K. Chen, Dr. X. Kong, X. Xie, J. Chen, Dr. X. Cao, Prof. S. Liang, Prof. A. Pan
State Key Laboratory of Powder Metallurgy,
School of Materials Science and Engineering,
Central South University,
Changsha, Hunan, 410083, P.R. China
E-mail: pananqiang@csu.edu.cn
[b] Prof. A. Pan
School of Physics Science and Technology,
Xinjiang University,
Urumqi, Xinjiang, 860046, P.R. China
[c] Dr. X. Kong
Institute of New Energy, College of Mechanical Engineering,
Hunan Institute of Science and Technology,
Yueyang, 414006, P.R. China

Batteries & Supercaps

Articles
doi.org/10.1002/batt.201900134

Chemistry Europe
European Chemical
Societies Publishing

charge and discharge process can be suppressed, further improving the structural stability of the composite material.

Herein, we report the in situ fabrication of sulfur-doped carbon wrapped $Fe_3O_4/Fe_7S_8/C$ nanoplates from Fe-MOF octahedra. As anode materials for lithium ion batteries, the $Fe_3O_4/Fe_7S_8/C$ nanoplates exhibit higher specific capacity, better cycle stability and rate capability than its counterparts. The smaller crystallites and the phase boundary are responsible for the improved electrochemical performances.

Experimental Section

Synthesis of Uniform Fe-MOF Octahedra

All the chemicals were used as received without further purification. The Fe-MOF octahedra is synthesized by a modified hydro-thermal method.[23] Briefly, 0.46 g of PTA (terephthalic acid) and 0.75 g of $FeCl_3 \cdot 6H_2O$ were dissolved in 120 mL of DMF (N,N-dimethylformamide) solution, followed by adding 4.8 mL of acetic acid. The mixture was then vigorously stirred for 1 hour to form a homogeneous orange solution. The obtained homogeneous solution was transferred to the Teflon-lined stainless steel autoclave, sealed and heated at 140 °C for 12 hours. After cooling down to room temperature naturally, the precipitate was collected by centrifugation and rinsed several times with deionized water and absolute ethanol, and then dried at 60 °C for further usage.

Synthesis of $Fe_3O_4/Fe_7S_8/C$, Fe_3O_4/C and Fe_7S_8/C

The sulfuration process is carried out in a tube furnace using sulfur powder as sulfur source. The synthesized Fe-MOF powder (0.1 g) and sulfur powder (0.5 g) were first annealed at 150 °C for 2 h to get good combination and then at 550 °C for another 4 h under Ar atmosphere at a heating rate of 5 °C min^{-1} to obtain $Fe_3O_4/Fe_7S_8/C$ composites. For comparison, Fe_7S_8/C and Fe_3O_4/C composites were prepared by using more sulfur (1.0 g) or without sulfur during the annealing process, respectively.

Material Characterizations

The crystalline phases of as-prepared samples were analyzed by X-ray diffractometer (XRD, Rigaku D/max 2500, CuKα, λ= 0.15405 nm). X-ray photoelectron spectroscopy (XPS) was obtained from ES§CALAB 250Xi (Thermo Fisher) and scanning electron microscopy (SEM, Quanta FEG 250,20 kV) was used to reveal the morphologies. Transmission electron microscopy (TEM, Titan G2 60–300 and JEOL JEM-2100F) was performed to get HRTEM images, SAED patterns, and energy dispersive spectrometer mapping. The nitrogen adsorption-desorption analysis was conducted at 77 k using a NOVA 2200e surface area and pore size analyzer (Quanta chrome Instruments). The carbon content of the $Fe_3O_4/Fe_7S_8/C$ is measured by carbon sulfur analyzer (CS600, American).

Electrochemical Measurements

All electrochemical measurements were performed using a half-cell (CR2016-type) assembled in an argon glove box. The working electrode was prepared by coating slurry onto Cu foil and dried at 80 °C for 12 hours, which was composed of the active material (70 wt%), super P (20 wt%) and sodium carboxymethyl cellulose (CMC, 10 wt%). The calculation of all the capacities is based on the total mass of the active materials ($Fe_3O_4/Fe_7S_8/C$, Fe_3O_4/C, Fe_7S_8/C).

And the mass loading of the active material in the electrode is around 1.5 mg cm^{-2}. Lithium foil and polypropylene membranes were used as the counter electrode and separator, respectively. 1 M $LiPF_6$ in ethylene carbonate (EC)-dimethyl carbonate (DMC)-diethyl carbonate (DEC) (1: 1: 1 in volume) were used as the electrolyte. Cyclic voltammetry (CV) tests (0.01–3.0 V vs Li/Li$^+$) were conducted on an electrochemical workstation (CHI660E, Shanghai Chenhua). A galvanostatic charge/discharge tests in a voltage range of 0.01–3.0 V was carried out using a Neware battery testing system (Neware CT-4008). The Electrochemical impedance spectroscopy (EIS) data were acquired using an Autolab electrochemical station (Metrohm) in the frequency range from 100 kHz to 0.1 Hz. The capacities of all cells were calculated based on the mass of the active material.

2. Results and Discussion

Scheme 1 illustrates the preparation process of sulfur-doped carbon wrapped $Fe_3O_4/Fe_7S_8/C$ nanocomposites. Uniform Fe-MOF octahedral precursor was firstly synthesized by a hydro-thermal method. It was then annealed at 150 °C for two hours at different fixed weight ratios of sulfur/Fe-MOF via a facile melt-diffusion strategy. And the obtained mixture was annealed at 550 °C for 4 h under Ar atmosphere to get the final products. During the annealing process at 550 °C, Fe-MOF precursor reacts with sulfur to produce $Fe_3O_4/Fe_7S_8/C$ heterogeneous composites, which were wrapped by sulfur-doped carbon matrix derived from organic framework. It is worth noting that octahedra has been converted into nanoplates during this process. The structural changes can be attributed to thermodynamically more stable state of the nanoplates for the obtained materials. The nanoplates morphology is believed of advantage for lithium ion storage because of its high surface exposure to the electrolyte and reduced lithium diffusion distance.[24] By adjusting the addition amount of sulfur during the annealing process, Fe_3O_4/C or Fe_7S_8/C nanoplates can be obtained. As indicated by Scheme 1b, the uniform sulfur-doped carbon coating layer can improve the electronic conductivity and structural stability of the composite. Moreover, the heterogeneous $Fe_3O_4/Fe_7S_8/C$ nanoplates have large phase boundary, which can improve the interfacial charge transfer. As anode materials for LIBs, it exhibits superior electrochemical performances, including high capacity and good rate capability.

Figure 1a shows the X-ray diffraction (XRD) patterns of the obtained samples by annealing Fe-MOF and sulfur powder in different mass ratios. When no sulfur was added, Fe_3O_4 can be obtained (PDF Card no. 19–0629). The main peaks at 35.46°, 56.94°, and 62.56° can be assigned to the (311), (422), and (511) planes of Fe_3O_4. When the mass ratio of Fe-MOF and sulfur powders was set as 1:5, heterogeneous Fe_3O_4 (PDF Card no.19-0629) and Fe_7S_8 (PDF Card no.25-0411) composites were obtained, indicating that the Fe-MOF is successfully converted into binary phases of Fe_3O_4 and Fe_7S_8. The corresponding peaks at 35.46°, 56.94°, and 62.56° can be ascribed to the (311), (422), and (511) planes of Fe_3O_4 and others corresponding peaks at 30.04°, 34.04°, 44.02°, 53.34°, and 71.7° can be assigned to the (200), (203), (206), (220) and (406) planes of Fe_7S_8. When the mass ratio of Fe-MOF and S powder was set to 1:10, all the
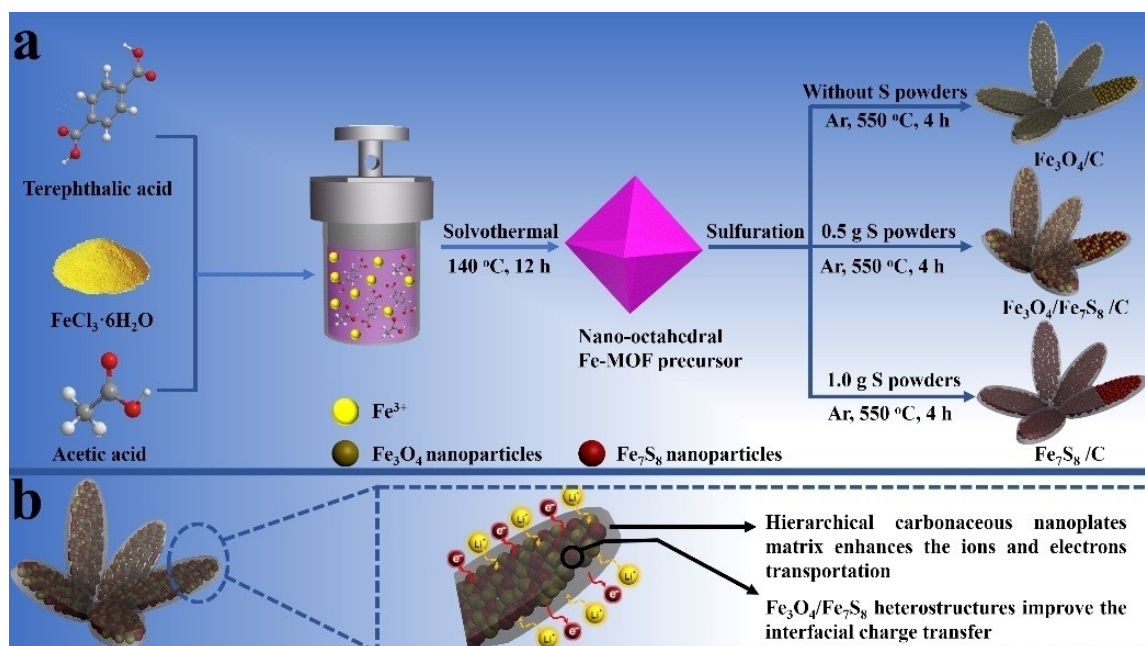
Scheme 1. Illustration of the fabrication of $Fe_3O_4/Fe_7S_8/C$ nanoplates (a) and the advantages of the structure (b).
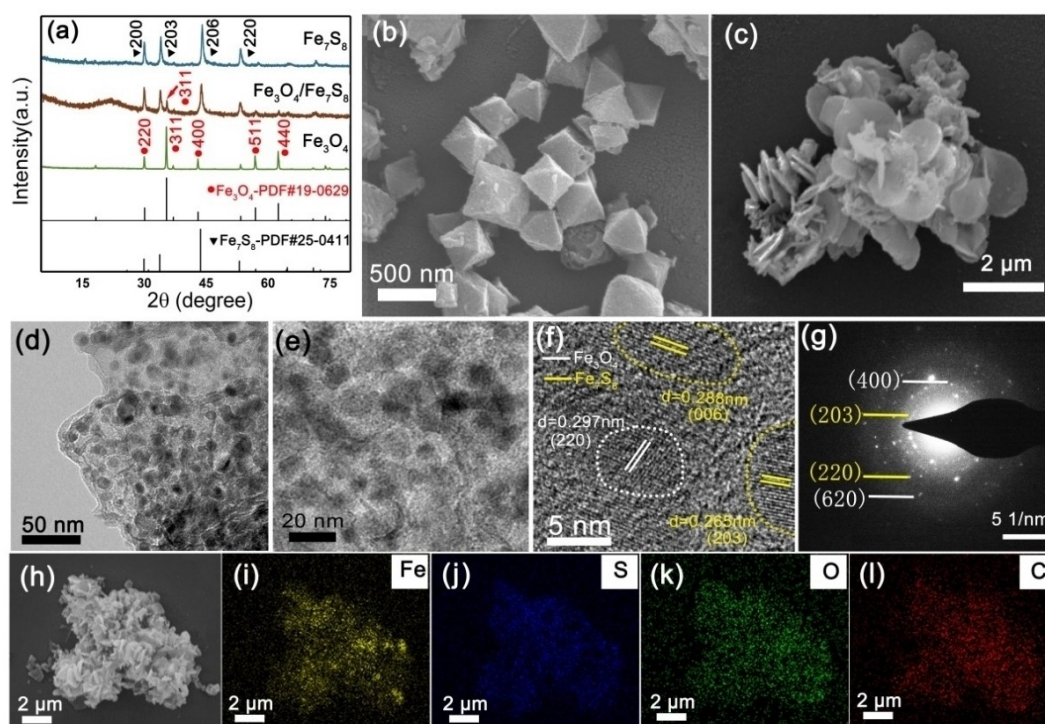
Figure 1. (a) XRD patterns of Fe_3O_4/C, $Fe_3O_4/Fe_7S_8/C$ and Fe_7S_8/C; (b) SEM image of Fe-MOF. (c) SEM image of $Fe_3O_4/Fe_7S_8/C$ nanoplates. (d, e) TEM, (f) HRTEM, and (g) SAED images of $Fe_3O_4/Fe_7S_8/C$; (h-l) the elemental mapping images of $Fe_3O_4/Fe_7S_8/C$ nanoplates.

diffraction peaks of the final product are completely assigned to the standard Fe_7S_8 (PDF Card no.25-0411). According to the result tested by carbon sulfur analyzer, the carbon contents of the $Fe_3O_4/Fe_7S_8/C$, Fe_3O_4/C and Fe_7S_8/C composites are 26%, 29% and 17%, respectively. Raman spectroscopy characterization (Figure S1) was also carried out to identify the carbon

component of the $Fe_3O_4/Fe_7S_8/C$ composite. The Raman diffraction peaks of G band ($\sim 1580\ cm^{-1}$) and D band ($\sim 1340\ cm^{-1}$) confirm the existence of carbon. Furthermore, the high I_D/I_G value (1.15) indicates that the amorphous carbon is dominant for $Fe_3O_4/Fe_7S_8/C$.

Figure 1b shows the morphology of the Fe-MOF octahedra in a width of 400–500 nm. The usage of acetic acid as the chemical inhibitor in the preparation of Fe-MOF can effectively control the size of Fe-MOF.[25] After annealing at 550 °C for 4 h, the octahedra were converted into nanoplates (Figure 1c). Fe_3O_4/C and Fe_7S_8/C nanoplates with similar morphology are obtained during the sulfurization process (Figure S2). Figure S3 shows the thermogravimetric analysis (TGA) curves of Fe-MOF precursor. A slight weight loss of 11.6% between room temperature and 252 °C can be ascribed to the evaporation of water in the composite, whereas the significant weight loss (47.6%) between 252 and 550 °C refers to the decomposition of metal-organic frameworks. After 550 °C, no obvious weight loss is detected, indicating that the decomposition reaction has almost completed. Therefore, 550 °C was chosen as the optimal temperature for the sulfuration process of Fe-MOF precursor. As shown in Figure 1d and Figure 1e, ultrafine nanoparticles about 5–20 nm in diameter are anchored on the Fe_3O_4/Fe_7S_8/C nanoplates. According to the HRTEM result (Figure 1f), the nanoparticles can be assigned to Fe_3O_4 and Fe_7S_8. The lattice fringes of 0.265 nm, 0.345 nm and 0.288 nm are corresponding to the interplanar spacings of (203), (110) and (006) planes of Fe_7S_8, respectively. And the interplanar spacing of approximately 0.253 nm and 0.287 nm belongs to the (311) and (220) crystal faces of Fe_3O_4, respectively. The selected area electron diffraction (SAED) pattern of the sample (Figure 1g) shows

bright crystal rings that matched well with the (400) and (620) planes of Fe_3O_4 and the (203) and (220) planes of Fe_7S_8. The SEM elemental mapping (Figure 1h–l) and the TEM elemental mapping images (Figure S4d-h) both indicate the uniform distribution of Fe, S, C and O elements in the nanoplates. For comparison, the nanocrystallites of Fe_3O_4 in Fe_3O_4/C nanoplates and Fe_7S_8 in Fe_7S_8/C nanoplates are about 20 nm in diameter (Figure S2). The difference of the crystallites can be attributed to the boundary phase of Fe_3O_4 and Fe_7S_8, which can hinder the continuous growth of the crystallites.

X-ray photoelectron spectroscopy (XPS) spectra were used to analyze the elemental composition and chemical state of the obtained samples. As shown in Figure S5, the overall XPS spectrum of Fe_3O_4/Fe_7S_8/C confirms the existence of Fe, S, C, and O elements. A high-resolution XPS spectrum of Fe 2p (Figure 2a) shows the peaks located at 712.8 eV and 719.2 eV ($2p_{3/2}$ with shake-up satellite), indicating the presence of Fe^{2+}, and the peaks at 710.8 eV ($2p_{3/2}$) and 724.9 eV ($2p_{1/2}$) are attributed to Fe^{3+}.[7] Figure 2b displays a high-resolution XPS spectrum of S 2p. Three peaks at 161.6 eV, 163.7 eV and 165.3 eV correspond to metal-sulfur (S^{2-}), while the weak broad peak centered at about 169.2 eV is possibly derived from the surface oxidation of sulfur or a strong interaction between sulfur and the carbon matrix.[26] The high resolution XPS spectrum of O 1s (Figure 2c) contains the peaks of Fe—O (530.1 eV) and O—S (530.9 eV). The existence of O—S bond
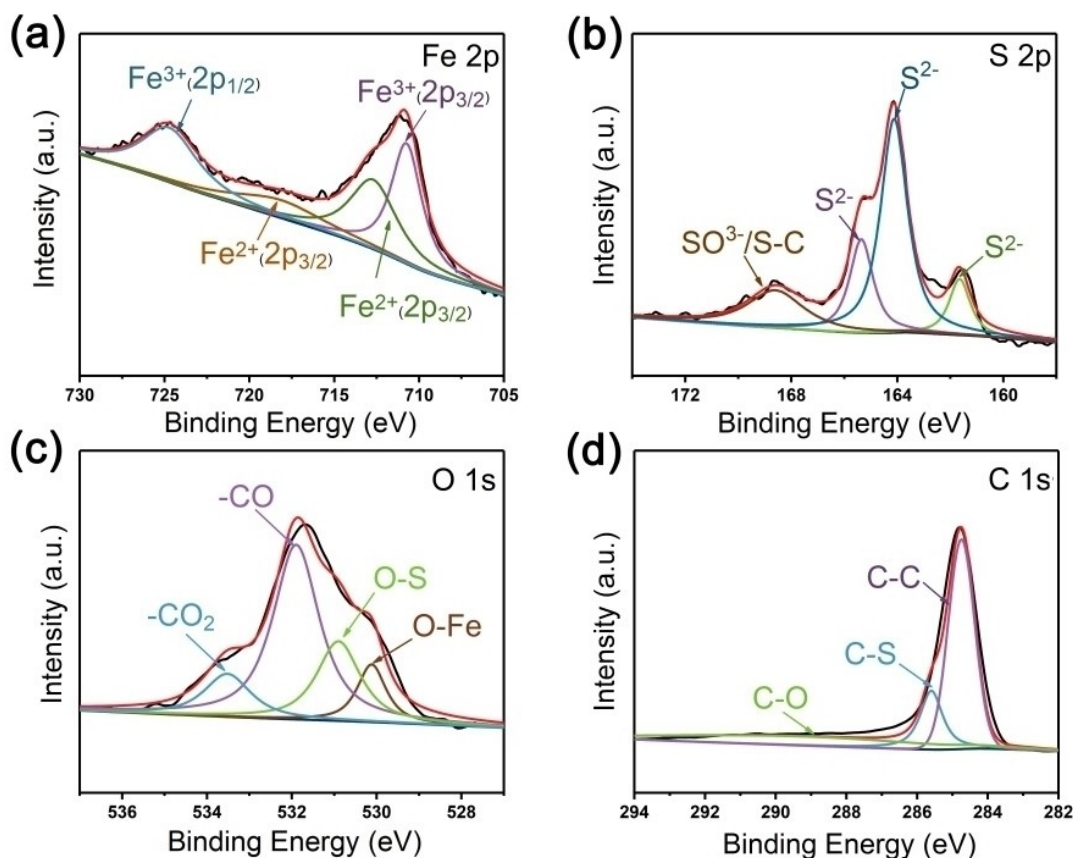
Figure 2. XPS spectra of Fe_3O_4/Fe_7S_8/C: High-resolution XPS spectrums of (a) Fe 2p; (b) S 2p; (c) O 1s; (d) C 1s.
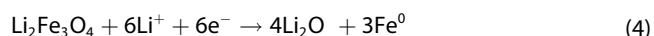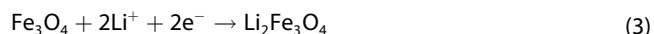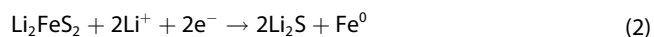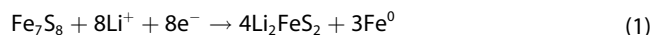
indicates that there is a chemical bond interaction between Fe_3O_4 and Fe_7S_8 in $Fe_3O_4/Fe_7S_8/C$ composite, which is beneficial to the structural stability of Fe_7S_8 during charge and discharge.[27–28] In the XPS spectrum of O 1s, the peak with a binding energy of 531.9 eV corresponds to −CO, and the other peak at 533.5 eV corresponds to -CO2. In the high resolution XPS spectrum of C 1s (Figure 2d), the peaks at 284.9, 285.6 and 289.2 eV correspond to C−C, C−S and C−O, respectively.[29]

In order to explore the specific surface area of the hierarchical $Fe_3O_4/Fe_7S_8/C$ nanoplates, nitrogen adsorption-desorption isotherm analysis was carried out. The Brunauer-Emmett-Teller (BET) test showed that the $Fe_3O_4/Fe_7S_8/C$ composite (Figure 3a) has a high specific surface area of $207\ m^2\,g^{-1}$ and pore volume of $0.33\ cm^3\,g^{-1}$ with a mean pore size of 3–4 nm. However, Fe_3O_4/C (Figure 3b) sample has much lower surface area ($164.7\ m^2\,g^{-1}$) and smaller pore volume ($0.31\ cm^3\,g^{-1}$). Fe_7S_8/C nanoplates (Figure 3c) have the smallest specific surface area ($121.5\ m^2\,g^{-1}$) and pore volume ($0.27\ cm^3\,g^{-1}$). The largest specific surface area of $Fe_3O_4/Fe_7S_8/C$ could be ascribed to its smaller nanocrystallites, pore size and narrower pore distribution. The porous structure and large specific surface area of the $Fe_3O_4/Fe_7S_8/C$ nanoplates can enlarge the effective contact area between the electrolyte and the electrode, shorten the diffusion path of the electrolyte ions and buffer the volume expansion during the charge-discharge process.
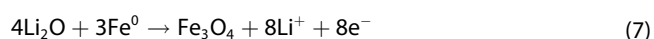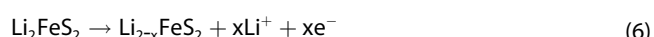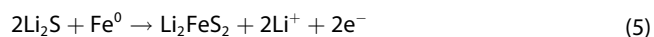
The electrode materials were assembled in CR2016 coin cells to evaluate their electrochemical performances and the result is shown in Figure 4. Figure 4a shows the initial five consequence cyclic voltammogram (CV) curves of the $Fe_3O_4/Fe_7S_8/C$ nanoplates at a scan rate of $0.1\ mV\,s^{-1}$. In the first cathodic scan, three cathode peaks at 0.72 V, 1.26 V and 1.65 V are detected. The sharp peak at 1.26 V can be attributed to the lithiation process of Fe_7S_8, which can be expressed as Equations (1, 2).[30–32] The plateau at 1.65 V is attributed to the formation of $Li_2Fe_3O_4$ (Equation 3).[33–34] In addition, the cathode peak at 0.72 V which transfer to 0.9 V in the subsequent cycle may attributed to the further lithiation process of $Li_2Fe_3O_4$ (Equation 4).[35] In the anodic scan, a sharp oxidation peak was observed at about 1.93 V, which is attributed to the formation of Li_2FeS_2 (Equation 5) and $Li_{2-x}FeS_2$ (Equation 6) by the Fe^0 conversion reaction, respectively.[36] The weak oxidation peak at 1.61 V is attributed to the transformation of Fe^0 into Fe_3O_4

(Equation 7).[33] The related electrochemical reactions could be described as follows:

Discharge process:

$$Fe_7S_8 + 8Li^+ + 8e^- \rightarrow 4Li_2FeS_2 + 3Fe^0 \quad (1)$$

$$Li_2FeS_2 + 2Li^+ + 2e^- \rightarrow 2Li_2S + Fe^0 \quad (2)$$

$$Fe_3O_4 + 2Li^+ + 2e^- \rightarrow Li_2Fe_3O_4 \quad (3)$$

$$Li_2Fe_3O_4 + 6Li^+ + 6e^- \rightarrow 4Li_2O + 3Fe^0 \quad (4)$$

Charge process:

$$2Li_2S + Fe^0 \rightarrow Li_2FeS_2 + 2Li^+ + 2e^- \quad (5)$$

$$Li_2FeS_2 \rightarrow Li_{2-x}FeS_2 + xLi^+ + xe^- \quad (6)$$

$$4Li_2O + 3Fe^0 \rightarrow Fe_3O_4 + 8Li^+ + 8e^- \quad (7)$$

The shift of the CV peaks in the second cycle is attributed to the partial irreversible side reactions and formation of unstable SEI films. The largely overlap of the CV curves of the later cycles indicate the good structural stability and phase reversibility of the heterogeneous composite nanoplates.

Figure 4b shows the galvanostatic discharge/charge curves of the 1st, 10th, 50th and 100th cycles of the $Fe_3O_4/Fe_7S_8/C$ nanoplates at a current density of $100\ mA\,g^{-1}$. During the first discharge process, two voltage platforms around 1.3 V and 0.7 V are detected and can be assigned to the lithium insertion into the electrode material. In the subsequent discharge process, the voltage platform is shifted to 1.4 V because of the irreversible reactions. During charging, a voltage platform at 1.9 V is ascribed to the oxidation process of Fe^0 to Li_2FeS_2. The galvanostatic discharge/charge curves of Fe_3O_4/C and Fe_7S_8/C are shown in Figure S6. As shown in Figure S6a, a distinct voltage plateau is identified at about 0.8 V in the initial discharge process, and shifts upward slightly in the subsequent cycle, which are similar to those reported for Fe_3O_4.[37–38] Figure S6b shows the discharge/charge curves of Fe_7S_8 nanoplates, which demonstrates lower initial capacity and poorer cycling stability.
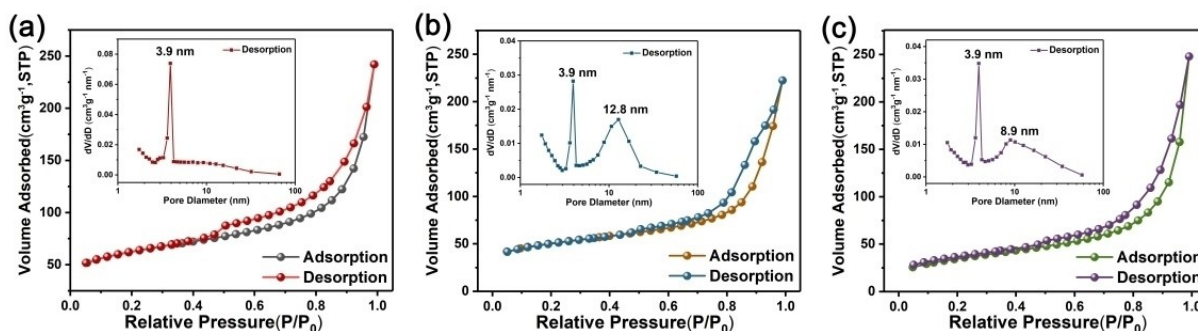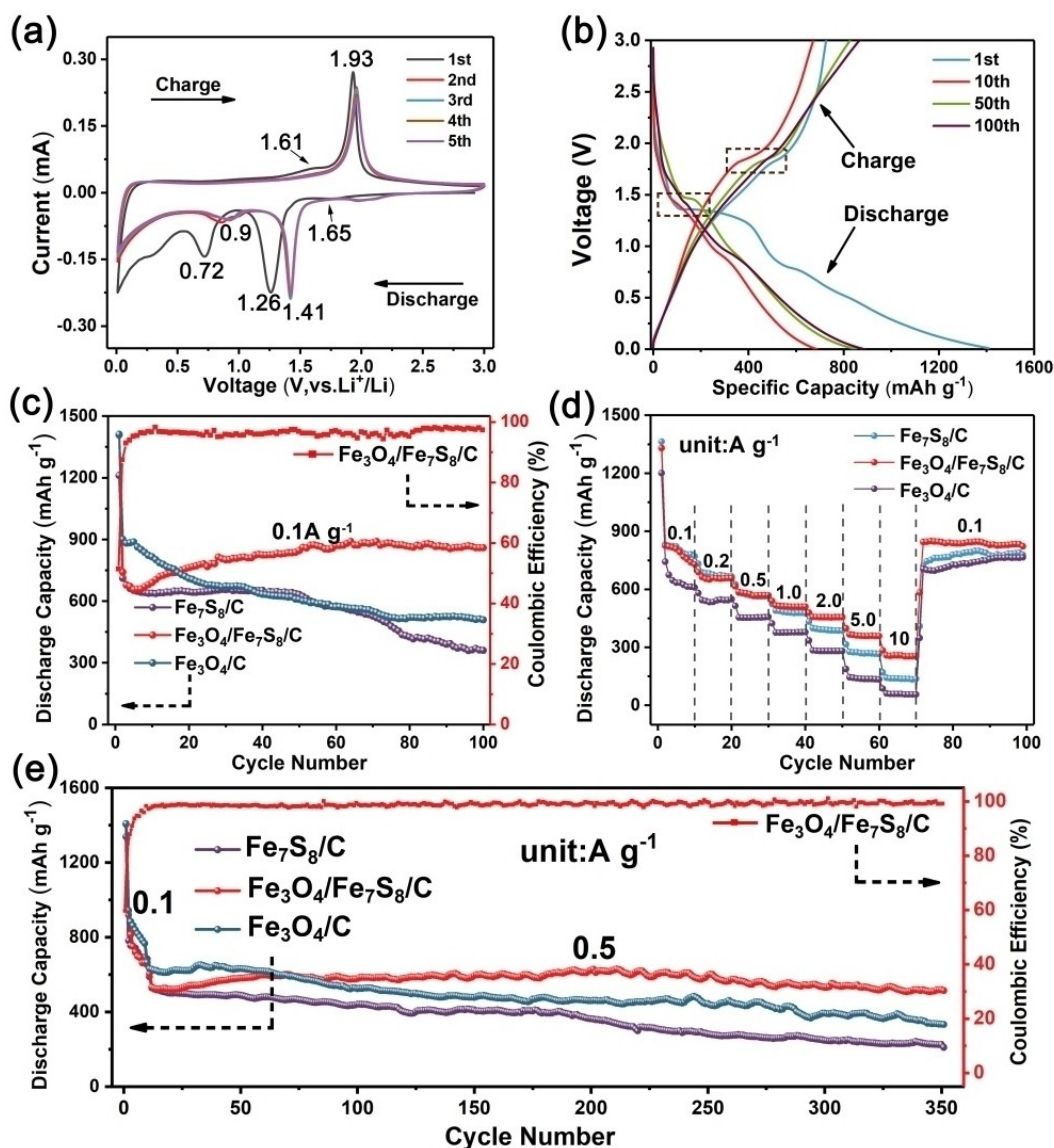

Figure 3. N_2 adsorption-desorption isotherms and pore size distribution of (a) the $Fe_3O_4/Fe_7S_8/C$, (b) the Fe_3O_4/C and (c) the Fe_7S_8/C.

Figure 4. Electrochemical performances of the obtained samples. (a) Initial five successive CV curves of $Fe_3O_4/Fe_7S_8/C$ electrode at 0.1 mV s^{-1}. (b) selected charge/discharge curves of 1st, 10th, 50th and 100th cycles of $Fe_3O_4/Fe_7S_8/C$ electrodes at the current density of 0.1 A g^{-1} between 0.1 and 3 V (vs Li/Li$^+$). (c) cycling performances of $Fe_3O_4/Fe_7S_8/C$, Fe_3O_4/C and Fe_7S_8/C electrodes at a current density of 100 mA g^{-1}, (d) rate performances and (e) long-term cycling stability of the electrodes at a current density of 0.5 A g^{-1}.

Figure 4c shows the cycling performances of Fe_3O_4/C, $Fe_3O_4/Fe_7S_8/C$ and Fe_7S_8/C nanoplates at 100 mA g^{-1} in the voltage range of 0.01-3.0 V vs. Li/Li$^+$. Among the three samples, Fe_3O_4/C had higher capacity than the other two samples at the initial stage, which can be attributed to its higher theoretical capacity. However, its discharge capacity decreased continuously and retain a specific capacity of only 508 mAh g^{-1} after 100 cycles. However, the capacity of the $Fe_3O_4/Fe_7S_8/C$ nanoplates decreases at the beginning and then started to increase and reached a stable capacity of 859 mAh g^{-1} after 100 cycles.[39] The cycling performance is much better than those of Fe_3O_4/C and Fe_7S_8/C. The superiority of the heterogeneous $Fe_3O_4/Fe_7S_8/C$ electrode would be attributed to the formation of stable solid electrolyte interphase layer, which is important to obtain good cycling performances. The construction of

heterogeneous phases can improve the diffusion kinetics of lithium ions, thereby, accelerating the lithium insertion/delithiation process.[40–41] On the other hand, the defects formed during cycling provide more active sites and promote reaction kinetics, which is also helpful for the lithium ions intercalation/deintercalation.[42] Figure 4d shows the rate performance of the as-prepared Fe_3O_4/C, $Fe_3O_4/Fe_7S_8/C$ and Fe_7S_8/C nanoplates. $Fe_3O_4/Fe_7S_8/C$ nanoplates delivered specific capacities of 755, 658, 567, 511, 454, 358 and 283 mAh g^{-1} at the current densities of 0.1, 0.2, 0.5, 1.0, 2.0, 5.0 and 10 A g^{-1}, respectively. When the current density was reset to 0.1 A g^{-1}, a capacity of 840 mA h g^{-1} can still be obtained with no obvious capacity fading. For comparison, the rate performances of Fe_3O_4/C and Fe_7S_8/C electrodes were much poorer. Figure 4e shows the long-term cycle performances of the electrodes at 0.5 A g^{-1}

after initial activation at the current density of 0.1 A g^{-1} for 10 cycles. The Fe$_3$O$_4$/Fe$_7$S$_8$/C can deliver a specific discharge capacity of 514 mAh g^{-1} after 350 cycles at the current density of 0.5 A g^{-1}, which is much higher than 332 mAh g^{-1} for Fe$_3$O$_4$/C and 210 mAh g^{-1} for Fe$_7$S$_8$/C nanoplates. The superior electrochemical performance of Fe$_3$O$_4$/Fe$_7$S$_8$/C nanoplates can be attributed to the following advantages: (1) The rich phase boundaries of the Fe$_3$O$_4$/Fe$_7$S$_8$/C composite can provide numerous extrinsic defects and active sites for rapid electrons and ions transportation. Moreover, the biphasic mixture helps to form small crystalline domains which can avoid deep solids diffusion and produce pseudocapacitance effect to increase lithium storage capacity; (2) Different lithium insertion potentials of Fe$_3$O$_4$ and Fe$_7$S$_8$ during charge and discharge process can buffer the overall volume expansion by means of synergistic effect; (3) Unique carbonaceous nanoplates effectively enhance the electrons conductivity and overall structural stability of the composite. Table S2 shows the electrochemical performance comparison results between Fe$_3$O$_4$/Fe$_7$S$_8$/C and previously reported Fe$_3$O$_4$ (Fe$_7$S$_8$)-based anode materials. The result indicates that our heterogeneous Fe$_3$O$_4$/Fe$_7$S$_8$/C nanoplates shows better electrochemical performance than other's works.

Electrochemical impedance spectroscopy (EIS) tests were further employed to investigate the Fe$_3$O$_4$/C, Fe$_3$O$_4$/Fe$_7$S$_8$/C and Fe$_7$S$_8$/C nanoplate electrodes. As shown in Figure 5, all the Nyquist plots (100 kHz to 0.01 Hz) show concave semicircle in the high frequency region and linear oblique line in the subsequent low frequency region. The corresponding equivalent circuit was shown Figure 5a and b (inset). R_s corresponds to the sum of the electrolyte resistance and the Ohmic resistance of the battery assembly, whereas R_f and CPE1 correspond to the resistance of SEI film and the constant phase element, respectively. R_{ct} represents the charge transfer resistance and CPE2 represents a double layer capacitor. The main

fitting parameters for the three samples are listed in Table S1. It is found that the R_{ct} of the Fe$_3$O$_4$/Fe$_7$S$_8$/C electrode is about 332.3 Ω, which is much smaller than those of Fe$_3$O$_4$/C (about 600.8 Ω) and Fe$_7$S$_8$/C (about 385.7 Ω), demonstrating that the Fe$_3$O$_4$/Fe$_7$S$_8$/C has the lowest charge transfer resistance. Moreover, the R_{ct} of the Fe$_3$O$_4$/Fe$_7$S$_8$/C electrode after 20 cycles at a current density of 100 mA g^{-1} is also measured and the value is about 128.4 Ω, smaller than that of the fresh battery, indicating the improved charge transfer kinetics of the electrode after cycling. The lower R_{ct} of Fe$_3$O$_4$/Fe$_7$S$_8$/C composite can be attributed to the porous carbonaceous nanoplates structure and the synergistic effect between Fe$_3$O$_4$ and Fe$_7$S$_8$, which can improve the electrons transportations.

The lithium reaction kinetics of Fe$_3$O$_4$/Fe$_7$S$_8$/C was further analyzed by (Galvanostatic Intermittent Titration Technique). Current pulse of 100 mA g^{-1} was applied for 30 minutes while the followed relaxation time is 60 minutes. The GITT measurement continues until coming to the cut-off voltage (0.01 V– 3.0 V). The Li$^+$ diffusion coefficients of the three samples were calculated according to the Equation S1, and the results of the first two cycles are shown in Figure 6. The diffusion coefficient varies at the course of discharge/charge, with the minima appears at the each redox plateau (Figure S8).[21] The increasing D values of Fe$_3$O$_4$/Fe$_7$S$_8$/C electrode can be ascribed to the capacitive storage with high kinetics[43] and the strong interactions of Li$^+$ with surrounding ions.[44] Fe$_3$O$_4$/Fe$_7$S$_8$/C exhibits higher Li$^+$ diffusion coefficient than Fe$_3$O$_4$/C and Fe$_7$S$_8$/C, which can be attributed to the smaller nanocrystallites of Fe$_3$O$_4$/Fe$_7$S$_8$/C and the rich phase boundaries between the two phases of Fe$_3$O$_4$ and Fe$_7$S$_8$, which can limit the growth of crystal domains and generate active sites of crystal defects and rapid ion diffusion, thus, accelerating Li$^+$ diffusions.

Cyclic voltammetry (CV) measurements were performed at different scan rates from 0.1 to 2.0 mV s^{-1} to evaluate capacitive contribution of Fe$_3$O$_4$/Fe$_7$S$_8$/C nanoplates. As shown in Fig-
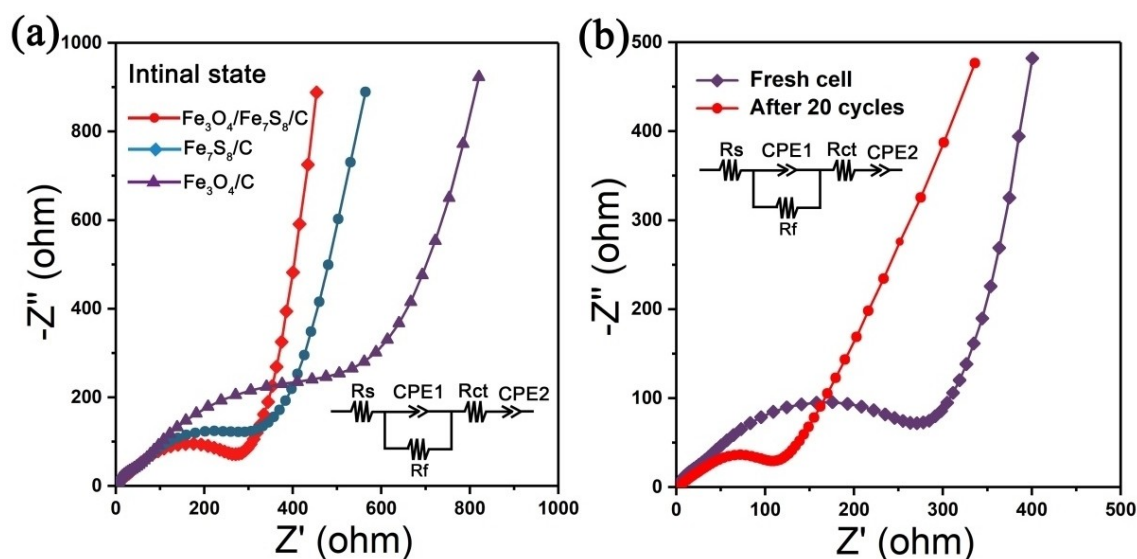
Figure 5. (a) Nyquist plots of the Fe$_3$O$_4$/C, Fe$_3$O$_4$/Fe$_7$S$_8$/C and Fe$_7$S$_8$/C electrodes measured at open-circuit potential of 0.01 Hz to 100 kHz. (b) Nyquist plots of the fresh Fe$_3$O$_4$/Fe$_7$S$_8$/C electrode and after 20 cycles (inset: the corresponding equivalent circuit).
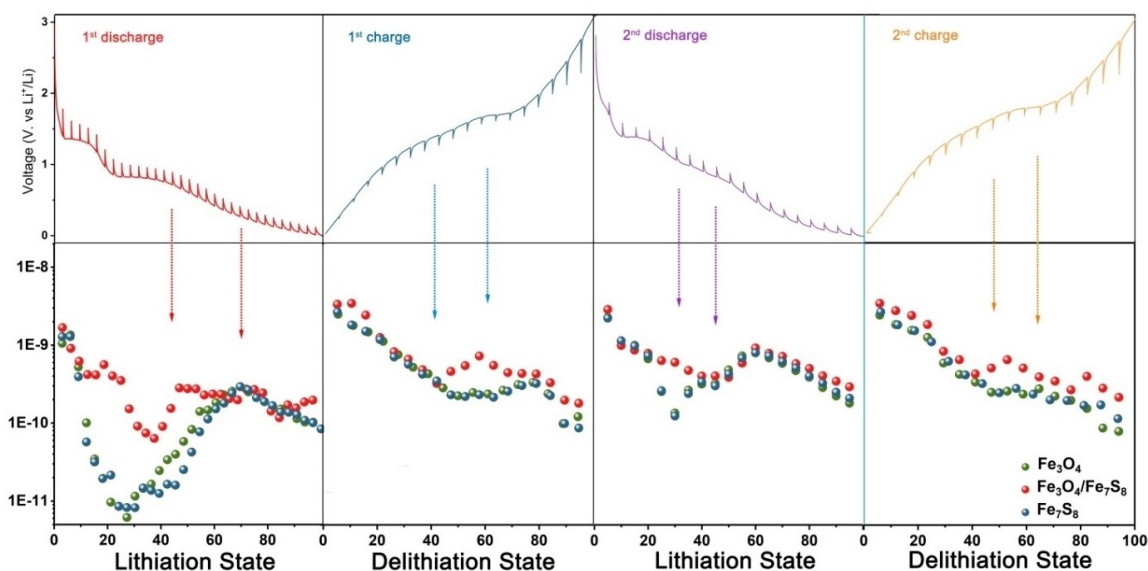
Figure 6. GITT curves and the corresponding value of Li$^+$ diffusion coefficient (D) at different discharge/charge state of Fe$_3$O$_4$/Fe$_7$S$_8$/C electrode.

ure 7a, the CV curves exhibit similar shapes when the scan rates are 0.1, 0.2, 0.6, 0.8, 1.0, 2.0 mV s^{-1}, respectively. The measured current (i) and the CV scan rate (v) obey the power-law relationship as shown in Equation (8):

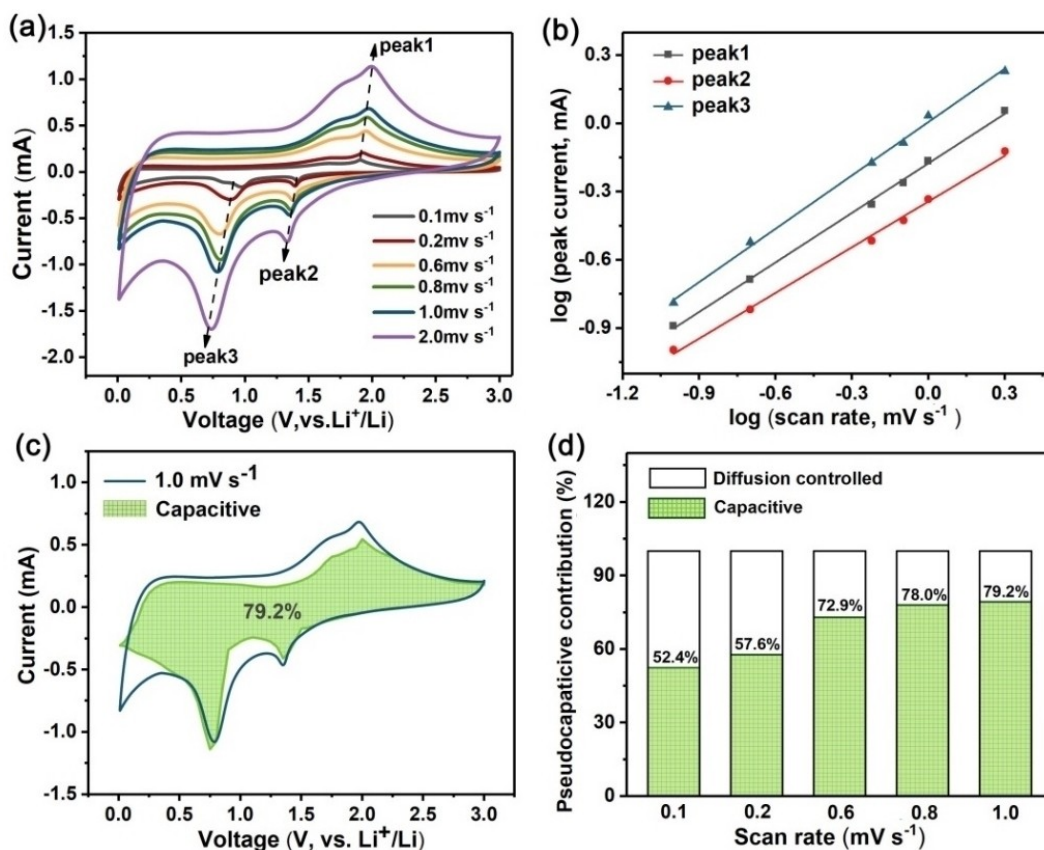**Figure 7.** Electrochemical kinetics analysis. (a) CV curves at different scan rates from 0.1 to 2.0 mV s^{-1}; (b) Corresponding log(i) versus log(v) plots at specific peak currents; (c) CV curve with the pseudocapacitive fraction shown by the shaded area at a scan rate of 1.0 mV s^{-1}. (d) The percent of pseudocapacitive contribution for Fe$_3$O$_4$/Fe$_7$S$_8$/C at different scan rates.

$$i = av^b \qquad (8)$$

where a and b are adjustable values. The *b* value can be calculated by Equation (8) and can be used to determine the charge storage mechanism. When the b value is 0.5, the reaction process is controlled by the diffusion mechanism, while high b value (1.0) means that the capacitance mechanism controls the reaction process. For peaks 1, 2 and 3 in Figure 7a, the corresponding *b* values obtained from the slopes in the log(*v*)-log(*i*) image (Figure 7b) are 0.73, 0.67 and 0.78, respectively. This indicates that the kinetics of the $Fe_3O_4/Fe_7S_8/C$ composite is controlled by both diffusion and capacitive process.[45] By dividing the current value (i) at a fixed potential (V) into two parts, capacitance control (k_1v) and diffusion control ($k_2v^{1/2}$) can be expressed by Equation (9):[46]

$$i(v) = k_1v + k_2v^{1/2} \qquad (9)$$

Where k_1 and k_2 are constants for a given potential. The green shaded area in the Figure 7c indicates that the contribution rate of $Fe_3O_4/Fe_7S_8/C$ at $1.0\ mV\,s^{-1}$ is 79.2%. The contribution rates of capacitance control and diffusion control at different scan rates were also calculated separately (Figure 7d). With the scan rate increasing, the pseudocapacitive capacitance contribution increased from 52.4% to 79.2%. The results indicate that the large capacity contribution from pseudocapacitive behavior of $Fe_3O_4/Fe_7S_8/C$ electrode.

3. Conclusions

In summary, hierarchical $Fe_3O_4/Fe_7S_8/C$ nanoplates were synthesized from hydrothermally prepared Fe-MOF octahedra during high-temperature annealing process. When utilized as anodes for LIBs, the heterogeneous $Fe_3O_4/Fe_7S_8/C$ composite exhibits superior lithium ion storage properties to Fe_3O_4/C and Fe_7S_8/C nanoplates. A reversible capacity of $859\ mA\,h\,g^{-1}$ can be remained for $Fe_3O_4/Fe_7S_8/C$ electrode after 100 cycles at a current density of $100\ mA\,g^{-1}$. Even at $2\ A\,g^{-1}$, the electrode still delivers a capacity of $549.3\ mA\,h\,g^{-1}$. The excellent electrochemical performance can be attributed to the carbonaceous porous nanoplates structure, smaller crystallites and binary boundaries of $Fe_3O_4/Fe_7S_8/C$. The results demonstrate that rational structural design and binary phase engineering can effectively improve the electrochemical performance of the anode materials for LIBs.

Conflict of Interest

The authors declare no conflict of interest.

[1] R. Huang, M. Huang, X. Li, F. An, N. Koratkar, Z. Z. Yu, *Adv. Mater.* **2018**, *30*, e1707025.
[2] C. Zhu, P. Kopold, W. Li, P. A. van Aken, J. Maier, Y. Yu, *Adv. Sci.* **2015**, *2*, 1500200.
[3] C. Han, X. Ren, Q. Li, W. Luo, L. Huang, L. Zhou, L. Mai, *Nano Res.* **2018**, *11*, 1285–1293.
[4] M. Wu, B. Xu, Y. Zhang, S. Qi, W. Ni, J. Hu, J. Ma, *Chem. Eng. J.* **2020**, *381*, 122558.
[5] L. Zhang, H. B. Wu, X. W. D. Lou, *Adv. Energy Mater.* **2014**, *4*, 1300958.
[6] X. Xie, Y. Hu, G. Fang, X. Cao, B. Yin, Y. Wang, S. Liang, G. Cao, A. Pan, *J. Mater. Chem. A* **2019**, *7*, 16541–16552.
[7] Q. He, K. Rui, J. Yang, Z. Wen, *ACS Appl. Mater. Interfaces* **2018**, *10*, 29476–29485.
[8] L. Shi, D. Li, J. Yu, H. Liu, Y. Zhao, H. Xin, Y. Lin, C. Lin, C. Li, C. Zhu, *J. Mater. Chem. A* **2018**, *6*, 7967–7976.
[9] Q. Ma, Q. Zhuang, J. Liang, Z. Zhang, J. Liu, H. Peng, C. Mao, G. Li, *Nanomaterials* **2017**, *7*. 7120431.
[10] Q. B. Zhang, J. Liao, M. Liao, J. Y. Dai, H. L. Ge, T. Duan, W. T. Yao, *Appl. Surf. Sci.* **2019**, *473*, 799–806.
[11] Y. Cai, G. Fang, J. Zhou, S. Liu, Z. Luo, A. Pan, G. Cao, S. Liang, *Nano Res.* **2017**, *11*, 449–463.
[12] Q. Wang, W. Zhang, C. Guo, Y. Liu, C. Wang, Z. Guo, *Adv. Funct. Mater.* **2017**, *27*, 1703390.
[13] D. Wu, C. Wang, M. Wu, Y. Chao, P. He, J. Ma, *J. Energy Chem.* **2020**, *43*, 24–32.
[14] B. Xu, S. Qi, M. Jin, X. Cai, L. Lai, Z. Sun, X. Han, Z. Lin, H. Shao, P. Peng, Z. Xiang, J. E. ten Elshof, R. Tan, C. Liu, Z. Zhang, X. Duan, J. Ma, *Chin. Chem. Lett.* **2019**, doi: 10.1016/ j.cclet.2019.10.028.
[15] X. Wei, W. Li, J. A. Shi, L. Gu, Y. Yu, *ACS Appl. Mater. Interfaces* **2015**, *7*, 27804–27809.
[16] Z. Chen, C. Wang, M. Chen, C. Ye, Z. Lin, L. Xing, Y. Liao, M. Xu, G. Cao, W. Li, *J. Mater. Chem. A* **2019**, *7*, 3924–3932.
[17] Y. Cai, X. Cao, Z. Luo, G. Fang, F. Liu, J. Zhou, A. Pan, S. Liang, *Adv. Sci.* **2018**, *5*, 1800680.
[18] B. Yin, X. X. Cao, A. Q. Pan, Z. G. Luo, S. Dinesh, J. D. Lin, Y. Tang, S. Q. Liang, G. Z. Cao, *Adv. Sci.* **2018**, *5*, 1800829.
[19] Y. Wang, T. Zhu, Y. Zhang, X. Kong, S. Liang, G. Cao, A. Pan, *J. Mater. Chem. A* **2017**, *5*, 18448–18456.
[20] X. Zhong, H. Huan, X. Liu, Y. Yu, *Nano Res.* **2018**, *11*, 3702–3709.
[21] G. Fang, Z. Wu, J. Zhou, C. Zhu, X. Cao, T. Lin, Y. Chen, C. Wang, A. Pan, S. Liang, *Adv. Energy Mater.* **2018**, *8*, 5635–5645.
[22] Y. Zhang, Q. Su, W. Xu, G. Cao, Y. Wang, A. Pan, S. Liang, *Adv. Sci.* **2019**, *6*, 1900162.
[23] Y. Huang, D. Ding, M. Zhu, W. Meng, Y. Huang, F. Geng, J. Li, J. Lin, C. Tang, Z. Lei, Z. Zhang, C. Zhi, *Sci. Technol. Adv. Mater.* **2015**, *16*, 014801.
[24] Y. He, H. Zhuang, C. Lei, L. Lei, Y. Hou, Y. Mai, X. Feng, *Nano Today* **2019**, *24*, 103–119.
[25] M. H. Pham, G. T. Vuong, A. T. Vu, T. O. Do, *Langmuir* **2011**, *27*, 15261–15267.
[26] S. Niu, W. Lv, G. Zhou, H. Shi, X. Qin, C. Zheng, T. Zhou, C. Luo, Y. Deng, B. Li, F. Kang, Q.-H. Yang, *Nano Energy* **2016**, *30*, 138–145.
[27] J. X. Song, Z. X. Yu, M. L. Gordin, X. L. Li, H. S. Peng, D. H. Wang, *ACS Nano* **2015**, *9*, 11933–11941.
[28] F. Wan, H.-Y. Lu, X.-L. Wu, X. Yan, J.-Z. Guo, J.-P. Zhang, G. Wang, D.-X. Han, L. Niu, *Energy Storage Mater.* **2016**, *5*, 214–222.
[29] C. Lin, C. Niu, X. Xu, K. Li, Z. Cai, Y. Zhang, X. Wang, L. Qu, Y. Xu, L. Mai, *Phys. Chem. Chem. Phys.* **2016**, *18*, 22146–22153.
[30] W. Huang, S. Li, X. Cao, C. Hou, Z. Zhang, J. Feng, L. Ci, P. Si, Q. Chi, *ACS Sustainable Chem. Eng.* **2017**, *5*, 5039–5048.
[31] S.-B. Son, T. A. Yersak, D. M. Piper, S. C. Kim, C. S. Kang, J. S. Cho, S.-S. Suh, Y.-U. Kim, K. H. Oh, S.-H. Lee, *Adv. Energy Mater.* **2014**, *4*, 1300961.
[32] Y. Xu, W. Li, F. Zhang, X. Zhang, W. Zhang, C.-S. Lee, Y. Tang, *J. Mater. Chem. A* **2016**, *4*, 3697–3703.
[33] C. He, S. Wu, N. Zhao, C. Shi, E. Liu, J. Li, *ACS Nano* **2013**, *7*, 4459–4469.

[34] M. Zhao, Z. Lian, Z. Long, B. Fu, R. Gao, S. Li, Y.-N. Zhou, Y. Song, *Appl. Surf. Sci.* **2019**, *481*, 1352–1359.

[35] L. Pan, X.-D. Zhu, X.-M. Xie, Y.-T. Liu, *J. Mater. Chem. A* **2015**, *3*, 2726–2733.

[36] B. Wu, H. Song, J. Zhou, X. Chen, *Chem. Commun.* **2011**, *47*, 8653–8655.

[37] B. Wang, H. B. Wu, L. Zhang, X. W. Lou, *Angew. Chem. Int. Ed. Engl.* **2013**, *52*, 4165–4168.

[38] W.-M. Zhang, X.-L. Wu, J.-S. Hu, Y.-G. Guo, L.-J. Wan, *Adv. Funct. Mater.* **2008**, *18*, 3941–3946.

[39] X. Kong, T. Zhu, F. Cheng, M. Zhu, X. Cao, S. Liang, G. Cao, A. Pan, *ACS Appl. Mater. Interfaces* **2018**, *10*, 8730–8738.

[40] G. Fang, Q. Wang, J. Zhou, Y. Lei, Z. Chen, Z. Wang, A. Pan, S. Liang, *ACS Nano* **2019**, *13*, 5635–5645.

[41] W. Luo, F. Li, Q. Li, X. Wang, W. Yang, L. Zhou, L. Mai, *ACS Appl. Mater. Interfaces* **2018**, *10*, 7201–7207.

[42] J. C. Guo, Q. Liu, C. S. Wang, M. R. Zachariah, *Adv. Funct. Mater.* **2012**, *22*, 803–811.

[43] V. Augustyn, J. Come, M. A. Lowe, J. W. Kim, P. L. Taberna, S. H. Tolbert, H. D. Abruna, P. Simon, B. Dunn, *Nat. Mater.* **2013**, *12*, 518–522.

[44] X. H. Rui, N. Ding, J. Liu, C. Li, C. H. Chen, *Electrochim. Acta* **2010**, *55*, 2384–2390.

[45] V. Augustyn, J. Come, M. A. Lowe, J. W. Kim, P. L. Taberna, S. H. Tolbert, H. D. Abruna, P. Simon, B. Dunn, *Nat. Mater.* **2013**, *12*, 518–522.

[46] L. Shen, H. Lv, S. Chen, P. Kopold, P. A. van Aken, X. Wu, J. Maier, Y. Yu, *Adv. Mater.* **2017**, *29.* 1700142.